Assessing the spatial and field dependence of the critical current density in YBCO bulk superconductors by scanning Hall probes

F Hengstberger, M Eisterer, M Zehetmayer and H W Weber

Atomic Institute of the Austrian Universities, Vienna University of Technology, Stadionallee 2,
1020 Vienna, Austria

E-mail: hengstb@ati.ac.at

Abstract

Although the flux density map of a bulk superconductor provides in principle sufficient information for calculating the magnitude and the direction of the supercurrent flow, the inversion of the Biot–Savart law is ill conditioned for thick samples, thus rendering this method unsuitable for state of the art bulk superconductors. If a thin (<1 mm) slab is cut from the bulk, the inversion is reasonably well conditioned and the variation of the critical current density in the sample can be calculated with adequate spatial resolution. Therefore a novel procedure is employed, which exploits the symmetry of the problem and solves the equations non-iteratively, assuming a planar thickness-independent current density. The calculated current density at a certain position is found to depend on the magnetic induction. In this way the average field dependence of the critical current density $J_c(B)$ is also obtained at low fields, which is not accessible to magnetization measurements due to the self-field of the sample. It is further shown that an evaluation of magnetization loops, taking the self-field into account, results in a similar dependence in the field range accessible to this experiment.

(Some figures in this article are in colour only in the electronic version)

1. Introduction

At present, bulk superconductors several centimetres in diameter and about one centimetre in thickness, trapping remanent magnetic fields exceeding 1 T at 77 K, can be reproducibly grown [1]. Texturing of the monolith is achieved by top seeded melt texture growth (TSMG), where crystallization evolves from a seed crystal placed on top of the bulk. Five growth sectors are formed, propagating from the facets of the crystal through the entire material [2]. The critical currents achieved in each growth sector, especially as a function of the seed distance, are therefore of particular interest.

A straightforward approach is to cut the sample and to characterize small pieces by magnetometry. However, this procedure is destructive and takes extensive measurement time. On the other hand, scanning Hall probe techniques can be employed to analyse the local properties of the bulk [3]. Among them the magnetoscan technique [4] proved to provide detailed information on the critical current flow on a local scale. However, even the strongest permanent magnets used in the magnetoscan device activate currents only in the uppermost layer of the bulk. The information refers to depths of less than 1 mm [5] and the inside of the bulk cannot be probed.

Currents flowing in the entire volume of the bulk can be activated by performing a (zero) field cooled hysteresis loop in a magnet. In principle sufficient data to calculate the current density on the sub-millimetre length scale, where substantial changes in J_c are expected, can be obtained from trapped field maps.

Although elaborate and numerically stable techniques exist [6–8], it was shown [9] that due to the large thickness of those samples the inverted matrix in such procedures is notoriously ill conditioned and can even be numerically

1
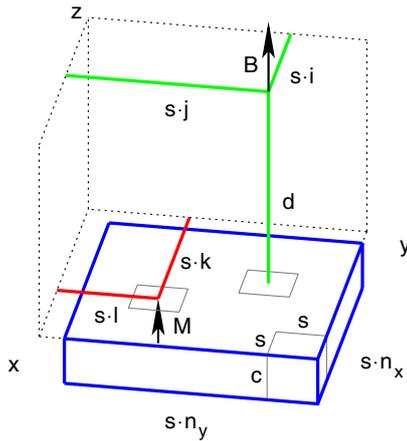
Figure 1. Coordinate system employed.

Figure 2. Estimate of the condition number for the parameters used in the experiment ($s = 0.2$ mm, $d = 0.55$ mm). Since the matrix exceeds the `Scilab` memory stack, the condition number was calculated for increasingly larger systems of up to 50×50 points. The convergence of the condition number is evident. Inset: symmetry of the matrix involved in the computation. The nine Toeplitz blocks constitute a block Toeplitz matrix.

singular. Thus, a reduction in thickness, either by grinding or preferably by cutting the bulk into discs, is mandatory to assess the local critical current distribution in this way. If the disc is sufficiently thin, a scanning mesh can be found which allows both an analysis of the current density on the sub-millimetre scale and a comparison to the magnetoscan signal at certain positions.

2. Numerics

2.1. General

In the coordinate system used in the following (cf figure 1) the top sample surface lies in the x, y-plane and the perpendicular component of the magnetic induction $B = \vec{B} \cdot \vec{e}_z$ is assessed. Similarly to [6], the current density is expressed as the curl of the magnetization density pointing in the z-direction, $\vec{J} = \vec{\nabla} \times M \vec{e}_z$. This implicitly satisfies current conservation, $\vec{\nabla} \cdot \vec{J} = 0$, for the z-independent planar current distribution $\vec{J}(x, y)$. Unlike in [6], the basic equation of the problem is derived by splitting the magnetic induction into two components and using a scalar magnetic potential (see the appendix for a detailed derivation). Discretization of the integral equation using cubic volume elements with constant M results in the two-dimensional (2D) matrix equation

$$\sum_{k=1}^{n_x} \sum_{l=1}^{n_y} K_{i,j,k,l} M_{k,l} = B_{i,j} \tag{1a}$$

$$K_{i,j,k,l} = F(\Delta x, \Delta y, \Delta z) \Big|_{s(i-k-\frac{1}{2})}^{s(i-k+\frac{1}{2})} \Big|_{s(j-l-\frac{1}{2})}^{s(j-l+\frac{1}{2})} \Big|_{d+c}^{d} \tag{1b}$$

$$F(\Delta x, \Delta y, \Delta z) = \frac{\mu_0}{4\pi} \tan^{-1} \left(\frac{\Delta x \, \Delta y}{\Delta z \sqrt{\Delta x^2 + \Delta y^2 + \Delta z^2}} \right). \tag{1c}$$

Here c denotes the sample thickness, d the distance between the active area of the Hall probe and the top sample surface (gap), s the step width, and $i, k = 1 \ldots n_x$, $j, l = 1 \ldots n_y$ the indices on the mesh; the antiderivative F is evaluated at the eight corners of the cubes in (1b).

Equation (1a) can be mapped one-to-one to one dimension by substituting $i' = i + j(n_x - 1)$, $k' = k + l(n_y - 1)$. The

equation now reads

$$\sum_{k'=1}^{n_x n_y} K'_{i',k'} M_{k'} = B_{i'} \tag{2}$$

and the problem can be tackled by matrix inversion algorithms.

As pointed out earlier, the matrix $K_{i,j,k,l}$ is in fact a Toeplitz block Toeplitz matrix [6]. This is a consequence of the translation invariance of the Biot–Savart law ($K_{i,j,k,l} = K_{|i-k|,0,|j-l|,0}$) and results in a highly symmetric matrix $K'_{i',k'}$ (cf the inset of figure 2). Therefore, both efficient storage and a fast algorithm for solving the system can be expected. However, [6] exploits the symmetry only for the storage of the matrix elements, and the method of conjugated gradients using the fast Fourier transform (FFT) is employed to solve the linear equation. Although the procedure is fast, employing an FFT [6, 7] implies the unnecessary assumption of periodicity in B outside the measurement area, which may create artefacts, if currents are flowing close to the edge of the scanning area.

Block Toeplitz matrices occur in a number of problems, such as image reconstruction or system identification. Fortunately, an efficient and fast algorithm, which exploits the symmetry of the structured matrix, is provided in [10][1]. The computation time is approximately 10 min for a 200×200 system on a desktop PC. This is presumably longer than FFT based algorithms, but still much less than the actual measurement time.

2.2. Condition number

The residuum of the solution is of the order of the machine error. However, it is shown in standard numerical algebra textbooks that matrix inversions can amplify a relative

---

[1] According to the online manual subroutine MB02ED uses 'Householder transformations, modified hyperbolic rotations and block Gaussian eliminations in the Schur algorithm to solve the linear equation'. All matrices were found to meet the prerequisite of being symmetric and numerically positive definite.

(measurement) error ϵ_B in the right-hand side of (2), leading to an unknown error in the calculated magnetization density ϵ_M. This behaviour is described by the condition number κ of a linear system:

$$\|\epsilon_M\|_2 \leqslant \kappa(K')\|\epsilon_B\|_2, \tag{3}$$

where the errors are measured in Euclidean norm. It was shown in [9] that the condition number of the inverted matrix is notoriously high for bulk superconductors. Therefore, special attention has to be paid to the choice of the step width s, defining $\kappa(K')$ at a given gap d. With a realistic distance d of about 0.15 mm (see section 3) and a sample thickness of 0.55 mm, the condition number was estimated using the numerical computation package `Scilab` [11] (cf figure 2).

As a rule of thumb one aims at a condition number κ such that

$$\|\epsilon_M\|_2 < 1 \tag{4}$$

holds. It was found that the matrix inversion is reasonably well conditioned as long as the step width is larger than the gap. The actual choice of $s = 0.2$ mm is adequate to resolve the spatial variations of the critical current on a sub-millimetre scale. The condition number $\kappa \approx 9$ combined with a rough estimate of the relative measurement error $\|\epsilon_B\|_2 \approx 0.01$ results in $\|\epsilon_M\|_2 \approx 0.09$, satisfying (4).

Calculating the current density involves computing a (numerical) derivative, which implies that the relative error in $\vec{J}(x, y)$ will be high, if the change in $M(x, y)$ (the current at this position) vanishes, as for example outside of the bulk or in defects. This is a peculiarity of measuring the relative error of a quantity close to zero. Note that the absolute error in $\vec{J}(x, y)$ is bounded by (3) and is expected to be acceptably low for most of the current distribution inside the sample as long as (4) holds.

3. Experimental details

A thin disc was cut from an undoped YBCO bulk superconductor with a diameter of 26.5 mm, which was grown by the top seeded melt growth technique [12], using a diamond saw. The cut was made near the upper surface of the bulk and the disc was polished with abrasive paper to a thickness of 0.55 mm.

Commercial Hall probes from Arepoc with active areas of 25×25 μm^2 (trapped field map) and 50×50 μm^2 (magnetoscan) were used in the experiments. All scans were carried out with a step width of 0.2 mm, which allows one to apply the inversion (see section 2.2).

For the trapped field maps a scanning area of 28 mm $\times$ 28 mm was used. The sample was field cooled in a split coil magnet in a field of 1.4 T. In order to minimize relaxation effects during the measurement, the scan was started 10 min after sweeping the magnetic field to zero. The temperature of the liquid nitrogen bath was recorded prior to and after the scans and was found to be 77.2 K, increasing due to oxygen uptake by about 0.1 K during the measurement. The resistive offset of the Hall probe was determined at the end of each measurement, with the Hall probe still immersed in liquid nitrogen, but at a large distance from the bulk.

A somewhat wider scanning area of 30 mm $\times$ 30 mm was used for the magnetoscans. This precaution was taken to assure that the magnet would not produce artefacts by stopping over the bulk after finishing a single line of the scan. The magnetoscan was carried out using a small SmCo permanent magnet of 2 mm in diameter, applying an induction of around 150 mT at the top sample surface of the bulk. Further details of the technique can be found in [4].

4. Results

4.1. Inversion of the trapped flux density profile

Assuming that the variation of the critical current over the sample thickness can be neglected immediately implies that the trapped field profiles recorded on the bottom and top surfaces are identical, which was confirmed by the experiment. The maxima of the trapped field were equal within one per cent on both sides of the bulk and found to be 252 mT. Strong negative fields of up to -100 mT were detected close to the edge of the sample, which result from the high diameter to thickness aspect ratio of the disc (cf figure 3(a)).

The high reproducibility between several measurements shows that the gap between the Hall probe and the sample surface (≈ 0.15 mm) remains unchanged in subsequent runs.

The inversion of the trapped flux density profile of the bottom surface of the disc is depicted in figure 3(b). Most of the bulk carries a current density of around 4×10^8 A m^{-2} in the remanent state. The defects (black arrows) close to the edge appear as regions where the critical current is drastically reduced, most likely due to cracks or large scale inclusions. A remarkable result of the inversion is the detection of the *c*-growth sector at the centre of the bulk. It is clearly displayed in the current density map as a rectangular area with low critical current density (dark region in the centre of the bulk (green region in the online version)).

In addition, a clear negative correlation between the critical current density and the magnitude of the perpendicular magnetic induction B is found, for example close to one of the *a–a* growth sector boundaries, where both the magnetic field and the current density change simultaneously (small white arrows). The correlation is most prominent at low fields, i.e., high current densities of up to 10^9 A m^{-2} flow close to the sample edge, where the magnetic induction changes sign and therefore $B \cong 0$. Moreover, a point inside the bulk (lowest white arrow) with reduced magnetic induction is reproducibly detected, where the current density significantly exceeds the nearby current densities. This demonstrates that a strong field dependence of the critical current is present, especially at low fields.

4.2. Comparison to magnetoscan

Due to the strong field dependence of the critical current, it is difficult to compare different regions of the bulk, as the self-field of the bulk is position dependent in the remanent state. In contrast, in the magnetoscan the background field of the permanent magnet is constant and the self-field is smaller,
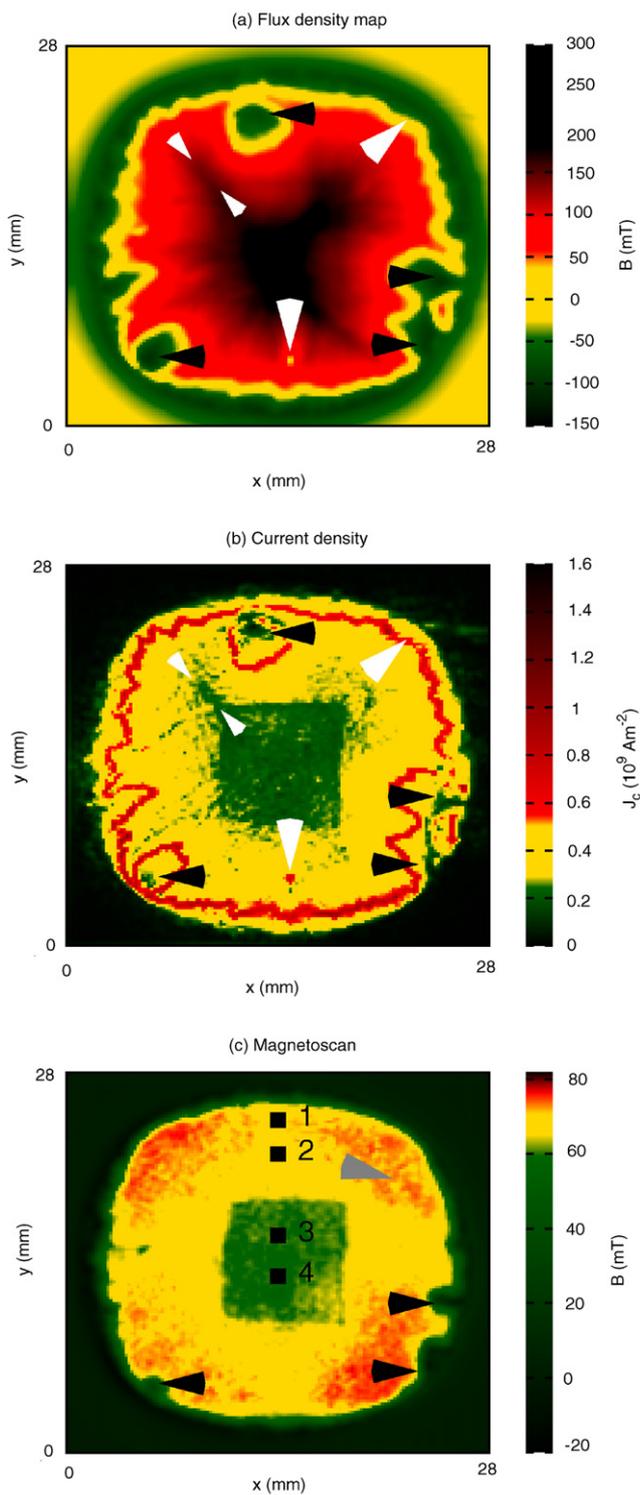
Figure 3. (a) A number of extended defects are detected in the trapped flux density map (black arrows) and strong negative fields of up to −100 mT are observed (dark area at the edge of the bulk (green area online)). (b) The inversion reveals a strong correlation between the magnetic induction and the current density (white arrows in (a), (b)). In the defects (black arrows) as well as in the *c*-axis growth sector (dark (green) rectangular area in the centre) the critical current density is significantly reduced. (c) The *c*-axis growth sector is again detected by the magnetoscan. The small length scale of the variations in the signal indicates strong local changes in the critical current (grey arrow). (The black rectangles indicate the cubes cut for magnetometry experiments.)
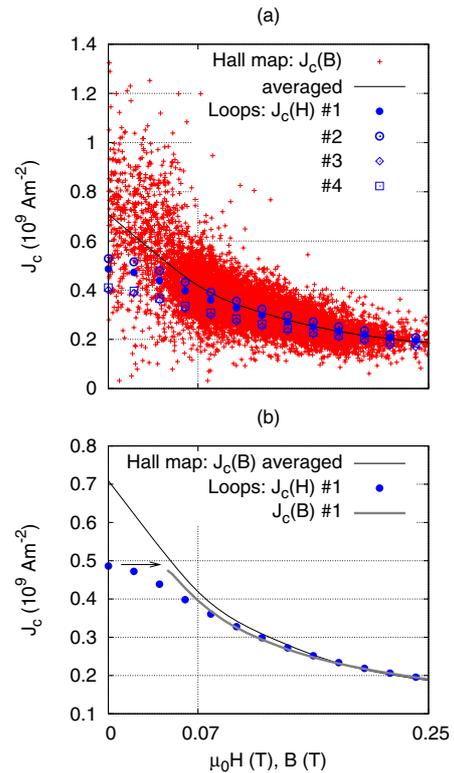
Figure 4. (a) $J_c(B > 0)$ correlation from the inversion, showing the average field dependence of the critical current density. The magnetization $J_c(H)$ data are similar to the smoothed data from the current calculation (black line) for high fields. The curves differ at low fields, because the self-field is not taken into account in the $J_c(H)$ data of the cubes. Further, the critical currents vary also from sample to sample in the magnetization data; the cubes cut from the seed area show the lowest critical current density. (b) Evaluation of the hysteresis loop for cube #1 taking the self-field into account. The field generated by the supercurrents in the sample shifts the applied magnetic induction to higher fields (arrow), resulting in a $J_c(B)$ dependence, which is now similar to the average data obtained from the current calculation. There is no indication for a flattening of the curve at small fields.

since the currents are activated only in an area of about the magnet's diameter [5].

All except one of the prominent defects are found in the magnetoscan (upper black arrow in figure 3). A possible explanation would be a large defect or inclusion at a depth that exceeds the penetration depth of the permanent magnet. Similar to the inversion, the reduction of the critical current is evident from the low magnetic response in the *c*-axis growth sector. Moreover, the observable granularity on a sub-millimetre scale of the bulk's response indicates strong local variations in the critical current density.

4.3. Comparison to magnetometry

The calculated current densities can be correlated with the *z*-component of the magnetic induction at their position. For this purpose the magnetic induction in the central plane inside the bulk was calculated after the inversion (see the appendix), resulting in a $J_c(B)$ plot (cf figure 4). Only points with positive

induction $B > 0$ were considered, which effectively cuts off the noise due to the extended defects close to the sample edge.

For comparison four cubes ($2 \times 2 \times 0.55$ mm^3) were cut from different positions of the bulk (cf figure 3(c)) and analysed in a SQUID magnetometer at the temperature of the liquid nitrogen bath during the previous scans. The magnetization loops were evaluated assuming the Bean model. A large sample to sample variation was found, the lowest critical current density being located at the c-axis growth sector in the centre of the bulk (cubes #3 and #4), in agreement with the above results. Although numerical errors in the inversion procedure (mainly due to the numerical derivation) cannot completely be excluded, the variation in the magnetization data elucidates the scatter in the calculated current densities, if one takes into account that the averaged volume is much larger in the SQUID measurements. This suggests that the scatter is primarily due to strong local variations of the critical current in the bulk, which is further supported by the granularity observed in the magnetoscan signal (cf figure 3(c)).

The average field dependence of the critical current density from the magnetization loops $J_c(H)$ shows good agreement with $J_c(B)$ obtained from the trapped flux density maps, except at low fields, where the curves clearly differ (cf figure 4(a)). This can be explained in terms of the sample's self-field, which is not considered in the evaluation of the magnetization experiment, since it takes only the externally applied field $\mu_0 H$ into account and neglects the field generated by the currents flowing in the sample.

To estimate this contribution the magnetoscan serves as a first approximation. This is because the currents are induced in an area determined by the magnet's diameter and therefore the volume of current flow mainly contributing to the magnetoscan signal is similar to the cubes used in magnetometry. Indeed the average induction of the magnetoscan (≈ 70 mT) is close to the field at which $J_c(H)$ and $J_c(B)$ start to differ.

For a more detailed analysis an evaluation method was applied (again based on the Bean model), which accounts for both the externally applied field and the mean self-field in the sample, thus providing an approximate $J_c(B)$ dependence [13]. Especially for low applied fields, where self-field effects become dominant, the evaluation shifts all data points to higher fields (cf figure 4(b)). This effect is particularly clear for the remanent state at zero applied field (arrow), where the magnetic induction is solely due to the trapped self-field. Consequently, a sample cannot be probed at zero magnetic induction by SQUID magnetization experiments.

When accounting for the self-field contribution, good agreement between the $J_c(B)$ curve from the SQUID loops and the average $J_c(B)$ curve from the inversion is found in the range accessible to the magnetization experiment (depicted in figure 4(b) for one of the cubes). Moreover, the field at which the correction starts to become effective and the self-field becomes important is equal to the simple estimate made above using the magnetoscan data (70 mT).

In contrast to SQUID magnetometry, the current calculation allows one to analyse the $J_c(B)$ dependence in fields ranging from zero induction to the maximum trapped field. A clear dependence of the critical current density on

the magnetic induction B is revealed in this way. There is no indication for a flattening in the average $J_c(B)$ at low fields.

5. Summary

The inversion of the Biot–Savart law represents an ill conditioned problem for bulk superconductors, but parameters, for example the step width of scan and the thickness of the sample, can be found which allow its application to thin discs cut from the sample. The matrix equation was solved without any additional assumptions by a fast algorithm, which exploits the symmetry of the problem. In this way, for example, the c-axis growth sector was clearly identified as a distinct region of low critical current density, a result which is also obtained by the magnetoscan and confirmed by magnetization measurements.

From a technological point of view both methods, the magnetoscan and the inversion of the flux density map, are complementary. The magnetoscan provides information on the local critical current density at a certain constant background field, which is of interest for superconducting bearings. On the other hand, information about the remanent current flow at the bulk's self-field is important for magnet applications and can be obtained by the inversion of the trapped flux density map of thin discs cut from the sample.

In addition, the current calculation was found also to provide the important average field dependence of the critical current at low fields (below the self-field), a region that is not accessible to magnetic measurements, even if the self-field is explicitly accounted for in the evaluation procedure. There is no indication of a plateau in $J_c(B)$, and the critical current density is also found to depend on the field in a continuous way at the lowest magnetic inductions.

Acknowledgments

Appendix

The magnetostatic Maxwell equations ($\vec{\nabla} \cdot \vec{B} = 0$ and Ampere's law $\vec{\nabla} \times \vec{B} = \mu_0 \vec{J}$) are treated by splitting the magnetic induction into a sum of two fields:

$$\vec{B} = \mu_0(\vec{\Omega} + \vec{M}), \qquad (A.1)$$

where $\vec{M}$ is chosen to satisfy the differential equation

$$\vec{\nabla} \times \vec{M} = \vec{J} \qquad (A.2)$$

in entire space, which satisfies current conservation, $\vec{\nabla} \cdot \vec{J} = 0$. Equation (A.2) defines $\vec{M}$ apart from a gradient field and an arbitrary constant, which are both chosen to be zero. Consequently $\vec{M}$ vanishes outside the sample and can therefore be interpreted as a magnetization, which is confined to the sample volume and establishes the current density $\vec{J}$ by spatial variations. Ampere's law results now in a homogeneous

equation for the field $\vec{\Omega}$:

$$\vec{\nabla} \times \vec{\Omega} = \vec{J} - \vec{\nabla} \times \vec{M} = 0, \qquad (A.3)$$

which can thus be derived from a scalar potential:

$$-\vec{\nabla}\Phi = \vec{\Omega}. \qquad (A.4)$$

Taking the divergence of this expression and substituting the second Maxwell equation ($\vec{\nabla} \cdot \vec{B} = \vec{\nabla} \cdot (\vec{\Omega} + \vec{M}) = 0$) results in

$$\vec{\nabla}^2\Phi = \vec{\nabla} \cdot \vec{M}, \qquad (A.5)$$

and the problem can be solved by the method of Green's functions:

$$\Phi(\vec{r}) = -\frac{1}{4\pi} \int dV' \frac{\vec{\nabla}' \cdot \vec{M}(\vec{r}\,')}{|\vec{r} - \vec{r}\,'|} + \frac{1}{4\pi} \oint d\vec{f}\,' \cdot \frac{\vec{M}(\vec{r}\,')}{|\vec{r} - \vec{r}\,'|}. \qquad (A.6)$$

The planar z-independent current flow can be represented by $\vec{M} = M(x, y)\,\vec{e}_z$, and consequently the first term vanishes since $\vec{\nabla} \cdot \vec{M} = \partial_z M_z = 0$ in the sample volume. Further, only the surfaces perpendicular to $\vec{M}$ contribute to the second term. Using (A.6), the measured induction B is expressed solely as a function of M:

$$B(\vec{r}) = \mu_0 M(\vec{r})$$
$$+ \underbrace{\frac{\mu_0}{4\pi} \int \int dx'\, dy' \frac{M(x', y')\,\Delta z}{(\Delta x^2 + \Delta y^2 + \Delta z^2)^{3/2}} \Big|_{d+c}^{d}}_{\Omega(\vec{r})}. \qquad (A.7)$$

Here $\Delta x = x - x'$, $\Delta y = y - y'$, $\Delta z = z - z'$, and the notation for evaluating antiderivatives are used to indicate the positive contribution from the top ($z' = d$) surface and the negative contribution from the bottom ($z' = d + c$) surface.

Note that $\vec{\Omega}$ vanishes for the case of an infinitely long slab (zero demagnetization) as $\Delta z \to \infty$ in (A.7). In this case the induction is simply determined by the magnitude of $\vec{M}$ at a certain position and $\vec{B} = \mu_0 \vec{M}$ inside and $\vec{B} = 0$ outside the slab, where $\vec{M} = 0$. However, for finite geometries there will always be a contribution from $\vec{\Omega}$ in (A.7), and the relation between $\vec{B}$ and $\vec{M}$ is non-local. Therefore the integral equation (A.7) must be solved in order to attain $\vec{M}$.

The corresponding set of linear equations for the discrete measured data is formulated by approximating the sample as an array of cubes with constant M. Summing over all elements results in the matrix equation

$$\sum_{k=1}^{n_x} \sum_{l=1}^{n_y} K_{i,j,k,l} M_{k,l} = \mu_0 \Omega_{i,j} = B_{i,j}. \qquad (A.8)$$

Here, the matrix entries $K_{i,j,k,l}$ are calculated by evaluating the antiderivative

$$F(\Delta x, \Delta y, \Delta z)$$
$$= \frac{\mu_0}{4\pi} \int \int dx\, dy \frac{\Delta z}{(\Delta x^2 + \Delta y^2 + \Delta z^2)^{3/2}} \qquad (A.9)$$
$$= \frac{\mu_0}{4\pi} \tan^{-1}\left(\frac{\Delta x \Delta y}{\Delta z \sqrt{\Delta x^2 + \Delta y^2 + \Delta z^2}}\right) \qquad (A.10)$$

at the eight corners of the cubes:

$$K_{i,j,k,l} = F(\Delta x, \Delta y, \Delta z)\Big|_{s(i-k-\frac{1}{2})}^{s(i-k+\frac{1}{2})} \Big|_{s(j-l-\frac{1}{2})}^{s(j-l+\frac{1}{2})} \Big|_{d+c}^{d}. \qquad (A.11)$$

Once the components $M_{k,l}$ are obtained by inverting (A.8), the current density can be calculated by employing (A.2). Further, the induction at any distance d outside the sample can be obtained from (A.8). Note that the magnetic induction B in the central plane ($d = -c/2$) of the sample, which is needed to obtain $J_c(B)$, is given by

$$\mu_0 M_{i,j} + \sum_{k=1}^{n_x} \sum_{l=1}^{n_y} K_{i,j,k,l} M_{k,l} = \mu_0(M_{i,j} + \Omega_{i,j}) = B_{i,j} \qquad (A.12)$$

as M does not vanish inside the sample.

References

[1] Cardwell D A and Hari Babu N 2006 *Physica* C **445** 1–7
[2] Cardwell D A 1998 *Mater. Sci. Eng.* **53** 1–10
[3] Haindl S, Eisterer M, Hörhager N, Weber H W, Walter H, Shlyk L, Krabbes G, Hari Babu N and Cardwell D A 2005 *Physica* C **426** 625–31
[4] Eisterer M, Haindl S, Wojcik T and Weber H W 2003 *Supercond. Sci. Technol.* **16** 1282–5
[5] Zehetmayer M, Eisterer M and Weber H W 2006 *Supercond. Sci. Technol.* **19** 429–37
[6] Wijngaarden R J, Spoelder H J W, Surdenau R and Griessen R 1996 *Phys. Rev.* B **17** 6742–9
[7] Jooss C, Warthmann R, Forkl A and Kronmüller H 1998 *Physica* C **299** 215–30
[8] Carrera M, Amorós J, Obradors X and Fontcuberta J 2003 *Supercond. Sci. Technol.* **16** 1187–94
[9] Eisterer M 2005 *Supercond. Sci. Technol.* **18** 58–62
[10] http://www.icm.tu-bs.de/NICONET 2008
[11] http://www.scilab.org 2008 The condition number is obtained by computing the singular value decomposition (SVD) of the matrix
[12] Krabbes G *et al* 1995 *Physica* C **244** 145–52
[13] Wiesinger H P, Sauerzopf F M and Weber H W 1992 *Physica* C **203** 121–8